AD-A047 384 LOCKHEED MISSILES AND SPACE CO INC PALO ALTO CALIF PA--ETC F/G 4/1
MEASUREMENT OF SPATIAL STRUCTURE IN OPTICALLY THICK BARIUM ION --ETC(U)
MAY 77 R D SEARS, J B KUMER DNA001-76-C-0331
UNCLASSIFIED LMSC/D558734 DNA-4290F NL

1 OF 1
ADA047384

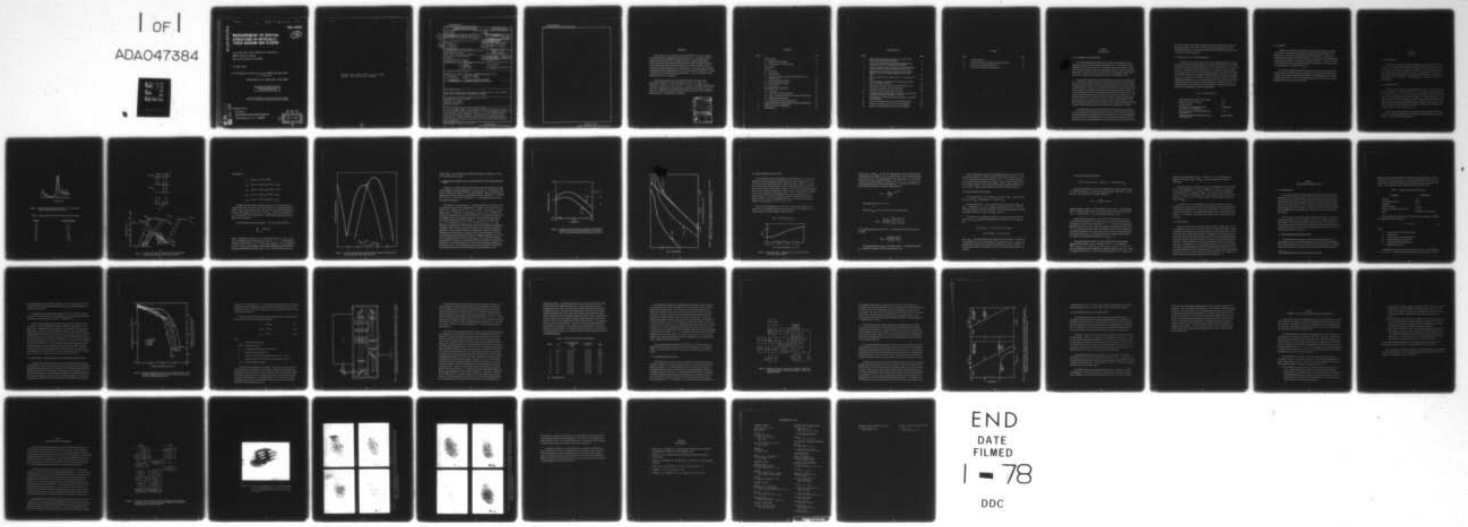

END
DATE FILMED
1-78
DDC

DNA 4290F

MEASUREMENT OF SPATIAL STRUCTURE IN OPTICALLY THICK BARIUM ION CLOUDS

Lockheed Palo Alto Research Laboratory
3251 Hanover Street
Palo Alto, California 94304

10 May 1977

Final Report for Period 1 July 1976—31 May 1977

CONTRACT No. DNA 001-76-C-0331

APPROVED FOR PUBLIC RELEASE;
DISTRIBUTION UNLIMITED.

THIS WORK SPONSORED BY THE DEFENSE NUCLEAR AGENCY
UNDER RDT&E RMSS CODE B322076462 L25AAXHX63510 H2590D.

Prepared for
Director
DEFENSE NUCLEAR AGENCY
Washington, D. C. 20305

Destroy this report when it is no longer needed. Do not return to sender.

UNCLASSIFIED

SECURITY CLASSIFICATION OF THIS PAGE (When Data Entered)

REPORT DOCUMENTATION PAGE

READ INSTRUCTIONS BEFORE COMPLETING FORM

1. REPORT NUMBER: DNA 4290F

2. GOVT ACCESSION NO.

3. RECIPIENT'S CATALOG NUMBER

4. TITLE (and Subtitle): MEASUREMENT OF SPATIAL STRUCTURE IN OPTICALLY THICK BARIUM ION CLOUDS.

5. TYPE OF REPORT & PERIOD COVERED: Final Report for Period 1 Jul 76 — 31 May 77

6. PERFORMING ORG. REPORT NUMBER: LMSC-D558734

7. AUTHOR(s): R. D. Sears, J. B. Kumer

8. CONTRACT OR GRANT NUMBER(s): DNA 001-76-C-0331

9. PERFORMING ORGANIZATION NAME AND ADDRESS:
Lockheed Palo Alto Research Laboratory
3251 Hanover Street
Palo Alto, California 94304

10. PROGRAM ELEMENT, PROJECT, TASK AREA & WORK UNIT NUMBERS: 62710H
Subtask L25AAXHX635-10

11. CONTROLLING OFFICE NAME AND ADDRESS:
Director
Defense Nuclear Agency
Washington, D. C. 20305

12. REPORT DATE: 10 May 1977

13. NUMBER OF PAGES: 48

14. MONITORING AGENCY NAME & ADDRESS (if different from Controlling Office): 145p.

15. SECURITY CLASS (of this report): UNCLASSIFIED

15a. DECLASSIFICATION/DOWNGRADING SCHEDULE

16. DISTRIBUTION STATEMENT (of this Report)

Approved for public release; distribution unlimited.

DNA, SBIE

4290F, AD-E300 029

17. DISTRIBUTION STATEMENT (of the abstract entered in Block 20, if different from Report)

18. SUPPLEMENTARY NOTES

This work sponsored by the Defense Nuclear Agency under RDT&E RMSS Code B322076462 L25AAXHX63510 H2590D.

19. KEY WORDS (Continue on reverse side if necessary and identify by block number)
Fabry-Perot Interferometer
Barium Ion Clouds
Optical Instruments
STRESS Program

20. ABSTRACT (Continue on reverse side if necessary and identify by block number)

A very high spatial and spectral resolution telescopic intensified Fabry-Perot Interferometer System (TIFIS) was designed, constructed, and fielded in support of the DNA STRESS program. The instrument was designed to make spatially resolved and spectrally resolved imaging measurements of upper atmospheric barium ion cloud releases conducted on the DNA STRESS program. The instrument design, operation, and quick-look data examples are presented.

DD FORM 1 JAN 73 1473 EDITION OF 1 NOV 65 IS OBSOLETE

UNCLASSIFIED

SECURITY CLASSIFICATION OF THIS PAGE (When Data Entered)

PREFACE

This is the final technical report on Contract DNA001-76-C-0331 covering the period of performance of 15 July 1976 through 31 May 1977. The purpose of the investigation reported herein was to design and fabricate a Telescopic Intensified Fabry-Perot Interferometer System (TIFIS) which was capable of making high spatial and spectrally resolved intensity measurements of the 4934 Å resonance scattered emission from high-altitude barium ion cloud releases. This report covers the design and fabrication of the TIFIS instrument as well as its operation at Tyndall AFB, Florida, in support of the DNA STRESS measurement program. A very brief summary of our quick-look results is also provided.

The principal investigator on this program was Robert D. Sears of the Electro-Optics Laboratory. Other contributors were Dr. J. B. Kumer, D. R. Hillendahl, E. Aamodt, R. Reeves, and Dr. S. B. Mende. The support and encouragement of our colleagues at the Lockheed Palo Alto Research Laboratory, as well as of Major B. W. Motal and his associates at DNA and the assistance of other STRESS program participants, are gratefully acknowledged.

CONTENTS

ILLUSTRATIONS

TABLES

Section 1
INTRODUCTION

1.1 STATEMENT OF THE PROBLEM

The DNA STRESS program addresses the problem of propagation of electromagnetic signals through a structured ionized region such as is produced by upper atmospheric releases of barium vapor. To generate and evaluate predictive models for the degradation effects produced on the propagated signal, two major experimental areas must be considered: adequate measurements of the propagation effects themselves, and a complete characterization of the ionized inhomogeneity region.

The spatial distribution of ionized irregularities in a barium vapor release and their column density along the direction of the viewing instrument can be determined by optical measurements of the resonantly scattered sunlight in one or more spectral wavelength regions. Because the ion cloud is optically thick in many of the observable spectral regions, measurement instrumentation requires high spectral resolution in order to deconvolve the effects of optical thickness upon the spectral line shape. The barium ion clouds exhibit hyperfine spectral structure because of isotope shift. This provides an opportunity to observe the cloud in an optically thinner emission region. Again, however, very high spectral resolution is required, approximately 0.01 Å. Such measurements have been made on previous barium releases (Operation SECEDE) by means of high-resolution Fabry-Perot interferometers (References 1 and 2).

The STRESS experiment requires the ability to obtain high spectral resolution as well as high spatial resolution such that the structure of the ionized cloud in dimensions perpendicular to the magnetic field can be characterized. Previous approaches utilized a Fabry-Perot interferometer as a spatial scanning instrument. However, because the small-scale inhomogeneities move, it appeared to be desirable to devise

an instrument which could combine spatial and spectral resolution requirements with imaging capabilities. Therefore, the TIFIS (Telescopic Intensified Fabry-Perot Interferometer System) was designed which incorporated both high spatial and spectral resolution with imaging capability.

1.2 DEFINITION OF THE TIFIS INSTRUMENT

To determine the characteristics required by the STRESS program for a spatial and spectrally resolved imaging instrument, a number of theoretical and experimental factors were considered. These design goals for the TIFIS instrument are summarized in Table 1. Development of the TIFIS instrument was undertaken with these design goals in mind, but also with the goal of utilizing certain DNA- and LMSC-owned optical and electronic components which greatly simplified design, construction, and reduced the cost. To summarize, the TIFIS was constructed mainly from DNA-owned optical components including the 18-in. Cassegrain telescope and Fabry-Perot interferometer. LMSC supplied much of the digital data processing and TV imaging apparatus. The TIFIS instrument was laboratory tested and then fielded at Tyndall AFB, Florida, in support of the STRESS events, BETTY through FERN.

Table 1. TIFIS design goals

Spatial Resolution at Cloud, 300-km Range	30 m
Spatial Field-of-View at Cloud	1 km
Pointing Accuracy	0.1°
Sensitivity to Cloud Radiance at 4934A (For 1 Pixel, 1-sec Integration)	10 kRayleigh
Spectral Resolution to Define 4934 Hyperfine Line Structure	0.01 A
Capability for Determining Spatial Structure on Moving Target	Imaging System

1.3 SUMMARY

In Section 2 is described the theoretical basis for making high spectral resolution irradiance measurements on the upper atmosphere barium ion clouds and for specifying the constraints affecting design of the TIFIS instrument. Details of the TIFIS instrument design are described in Section 3. A summary of the field operations and data acquisition phase of the program is included in Section 4. Finally, the results of a preliminary quick-look assessment of the data, based upon a very limited review of the imaging data, is presented in Section 5.

The measured TIFIS instrumental parameters plus our very quick-look assessment of the data to date indicate that useful high spatial and spectral resolution measurements were obtained for ionized inhomogeneities in the STRESS operation. Based upon the results to date, we believe that useful application of these data to the overall STRESS program goals will be accomplished.

Section 2
THEORY

2.1 INTRODUCTION

In this section we outline a method for obtaining the line-of-sight Ba^+ column density N from brightness measurements in which the hyperfine components in the Ba^+ 4934A line are resolved. Instrumental resolution 0.01A will sufficiently resolve the hyperfine lines. We will establish that the Ba^+ column density N may be accurately obtained from measurements of the hyperfine line brightnesses and their ratios provided that $N \lesssim 6 \times 10^{13}$ cm^{-2}. We do not expect N to exceed 3×10^{13} cm^{-2} in the experiment.

2.2 PERTINENT DATA

A high-resolution laboratory spectrum (Reference 3) of the Ba^+ resonance lines is shown in Figure 1. The relative abundances of Ba isotopes in naturally occurring Ba are shown in Table 2. The hyperfine structure and relative line intensities for the odd Ba^+ isotopes (Reference 4) are shown in Figure 2. The even isotopes have zero nuclear spin and therefore no hyperfine structure. The odd isotopes have nuclear spin 3/2 which results in the hyperfine splitting shown in Figure 2. From Figure 1, it is apparent that 0.01A FWHM resolution is sufficient to resolve the S_1 lines from the S_2 lines and the W lines from the S_3 lines.

From the relative intensities shown in Figure 2, and the oscillator strength reported by A. Gallagher (Reference 5), we compute the approximate line center optical depth $\tau_i = N/Noi$ for a line designated by i.

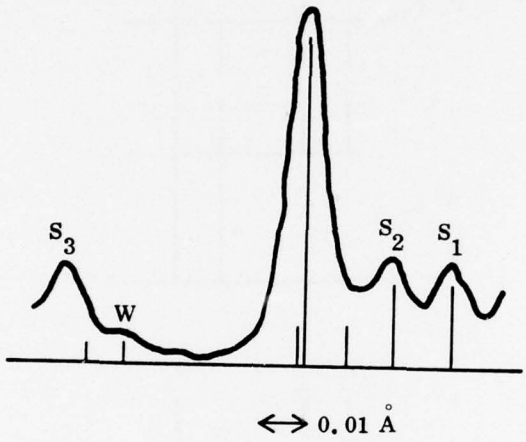

Figure 1. High-resolution laboratory spectrum of Ba^{+} 4934 Å lines showing various hyperfine components.

Table 2. Relative abundances of naturally occurring Ba isotopes

Isotope	Percent Abundance
138	71.83
137	11.25
136	7.74
135	6.56
134	2.42
132	0.096
130	0.103

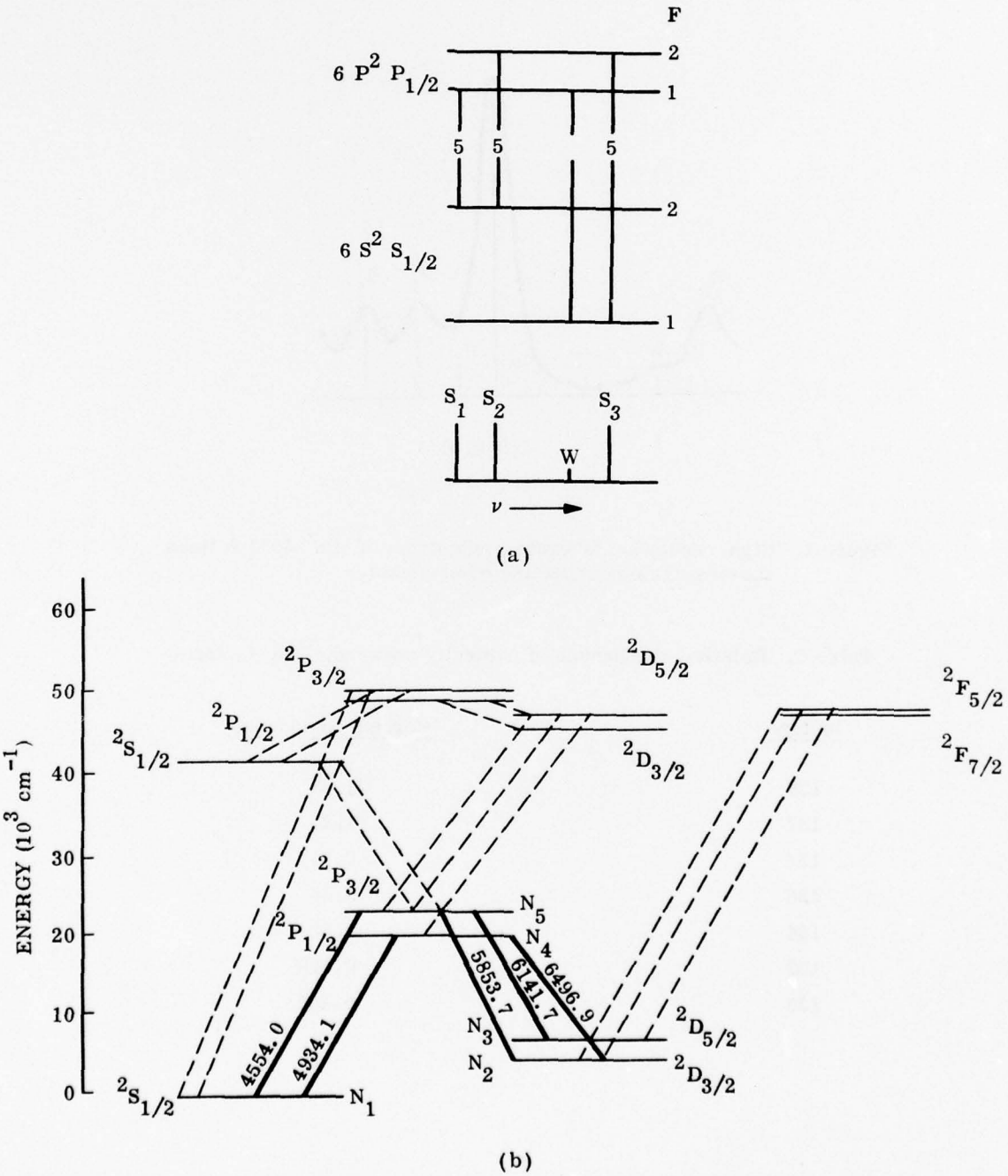

Figure 2. Energy level diagram for Ba II showing (a) hyperfine line structure and, (b) main resonance line transitions.

The results are:

$$\tau_8 = N/2.99 \times 10^{11} \text{ for } {}^{138}Ba^+$$

$$\tau_{S7} = N/6.00 \times 10^{12} \text{ for the } {}^{137}Ba^+ \text{ S lines}$$

$$\tau_{W7} = N/3.00 \times 10^{13} \text{ for the } {}^{137}Ba^+ \text{ W line}$$

$$\tau_{S5} = N/1.03 \times 10^{13} \text{ for the } {}^{135}Ba^+ \text{ S lines}$$

$$\tau_{W5} = N/5.17 \times 10^{13} \text{ for the } {}^{135}Ba^+ \text{ W line}$$

A Doppler line shape and an ionospheric temperature of 800 K were used to compute these values for the line center optical depths. In calculating these optical depths, we have assumed that for every ion in the $Ba^+ {}^2S_{1/2}$ ground state there are 0.74 more ions lurking in the $Ba^+ {}^2D_{5/2}$ and ${}^2D_{3/2}$ states as was calculated by R. W. Deuel and R. D. Sears (Reference 1). The pertinent partial energy level diagram is shown in Figure 2.

The optical depth at a given wavelength λ is the result of the summation

$$\sum \tau_i e^{-(\Delta\lambda_i/\lambda_D)^2}$$

where i designates the isotope and λ_i is the line center for line i, $\lambda_D \simeq 0.005A$ is the e-fold Doppler width of the line for 800 K and $\Delta\lambda_i = \lambda - \lambda_i$. The combined absorption line shape of the S_3 and W lines is shown in Figure 3. One can see that the S_3 and W lines are well separated. Since the full-width half-maximum (FWHM) of the proposed instrumental resolution ($\Delta\lambda_I = 0.01A$) is exactly equal to the e-fold

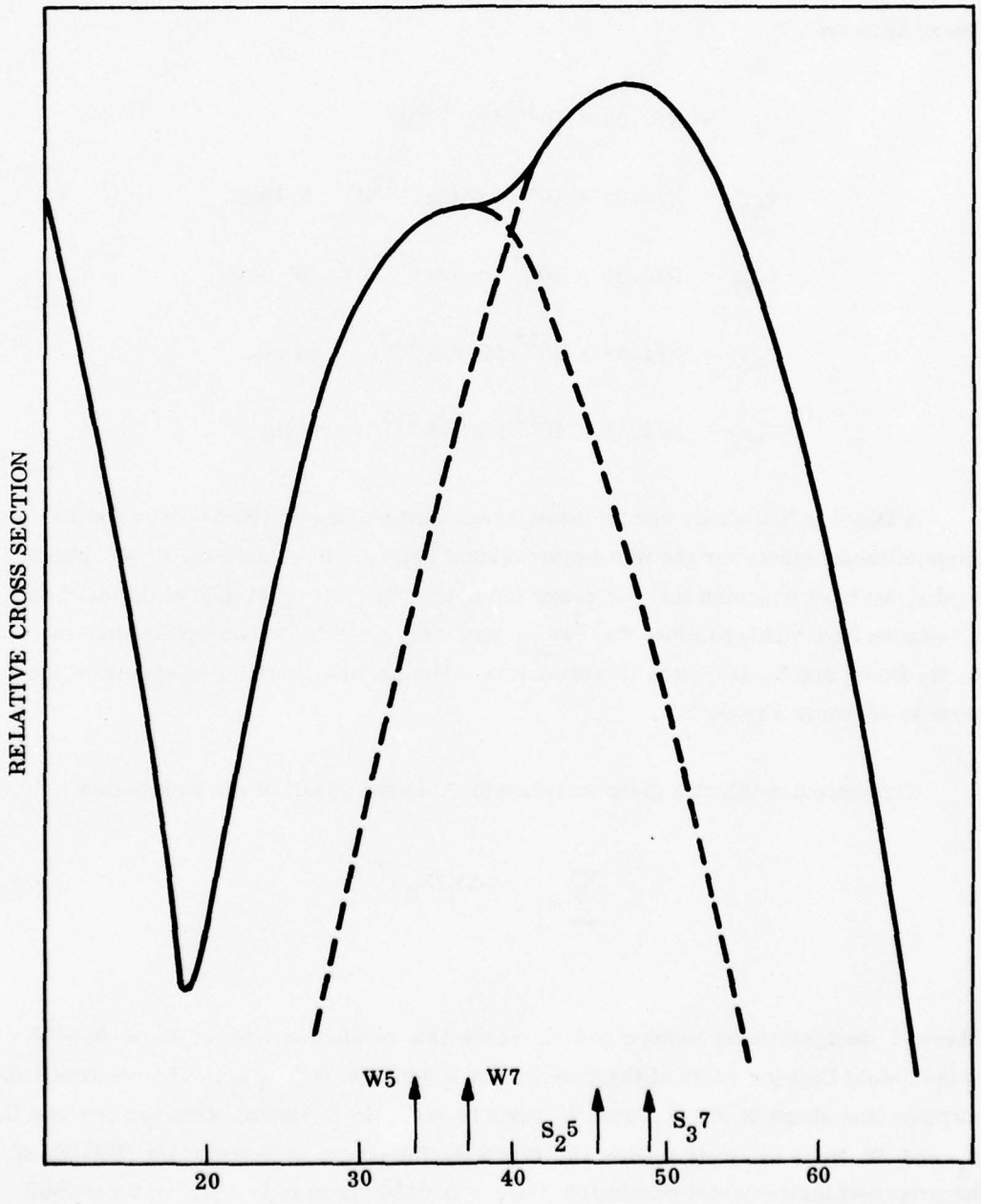

Figure 3. The Ba^+ absorption cross section plotted as a function of displacement from the main Ba^+ 4934 Å line (units mÅ).

Doppler width, it is obvious that this instrumental resolution is sufficient to resolve the W lines from the S_3 lines.

2.3 EXTRACTION OF LINE-OF-SIGHT COLUMN DENSITY FROM THE BRIGHTNESS DATA

In Figure 4 we plot the estimated time histories of the cloud center line-of-sight column densities for viewing transversely $N_\perp$ and parallel N_{11} to the magnetic field line for a release which yields 10^{25} ions at 185-km altitude. These time histories are estimated on the basis of transverse and parallel diffusion coefficients $D_\perp \simeq 0.02$ km^2 sec^{-1} and $D_{11} = 0.17$ km^2 sec^{-1} (Reference 6). A time constant of 30 sec for ion formation is also utilized.

From Figure 1 we can see that τ_W, the optical depth of the W lines, will not exceed unity for any time and viewing geometry. In Figure 5 we show the curves of growth $W(\tau_i)$ plotted versus N for i = 8, S7, and W7. The quantity τ_{W7} is also plotted versus N in Figure 5. By inspecting τ_{W7} and $W(\tau_{W7})$ in Figure 5 one sees that by assuming the cloud is optically thin in the W7 line and by analyzing the W7 line brightness data, using techniques suitable for the optically thin case, then one would expect to obtain the ion column density N, with an error of about 30% for $\tau_{W7} \simeq 1.0$ and about 10% for $\tau_{W7} \simeq 0.5$, and about 3% for $\tau_{W7} \simeq 0.1$. The technique for analyzing the W7 line brightness data on the optically thin assumption is essentially similar to that given by Deuel and Sears, whose analysis is contained in Reference 1. Their analysis would have to be modified to account for the hyperfine splitting of the odd isotope levels. However, this is a trivial adjustment. Thus we see by employing simple optically thin analysis to brightness measurements in the W line we can expect to obtain accuracy for the value of N to within 10% or better for viewing geometry transverse to the magnetic field and 30% or better for parallel viewing geometry. In the following section, we outline more sophisticated methods to obtain better accuracy. These methods also must be utilized in analysis of the data we expect to obtain in order to verify that the optically thin assumption is valid.

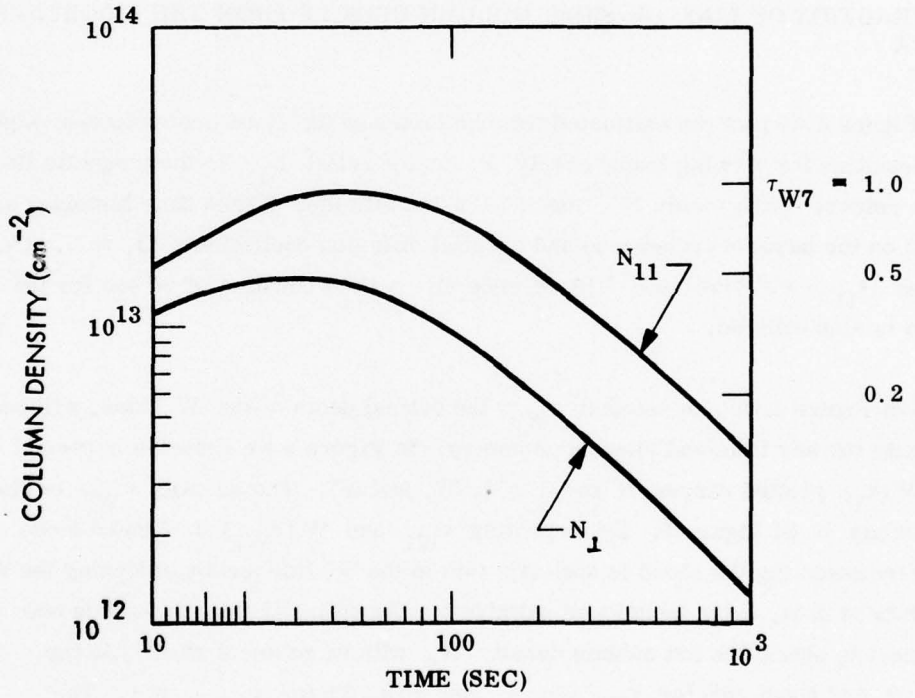

Figure 4. Estimates for the transverse and parallel (to the magnetic field) Ba^+ cloud center column densities as a function of time. The corresponding optical depth τ_{W7} is also shown.

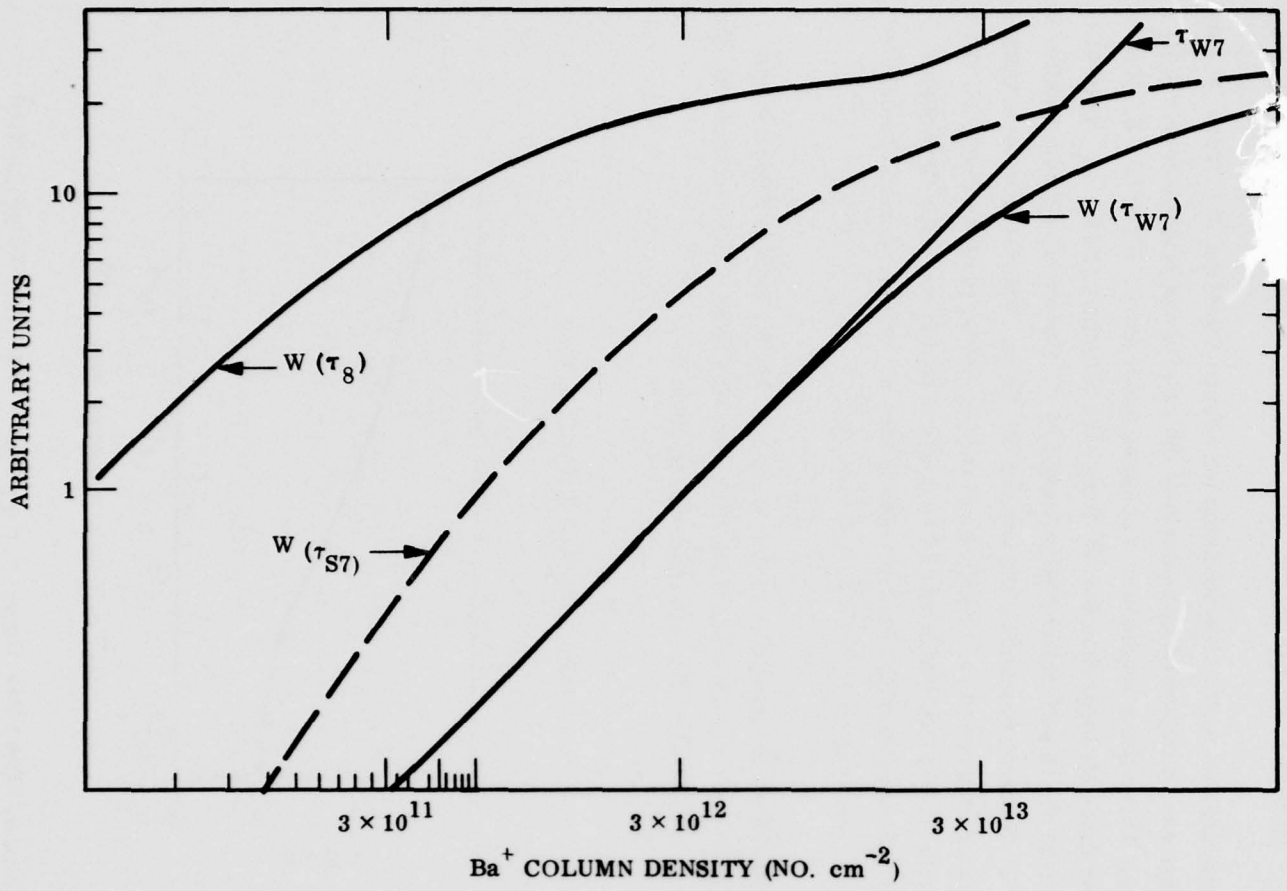

Figure 5. Curves of growth W (τi) plotted versus N for various Ba^+ lines. The optical depth τ_{W7} is plotted for purpose of comparison with W (τ_{W7}).

2.4 MORE SOPHISTICATED ANALYSIS

The optically thin method for obtaining ion column densities N, from W line brightness data can be improved by analysis of the ratio of the brightness in the S_1 and W lines. These lines originate in a common upper level. Since the S_1 lines are about five times stronger than the W lines, the brightness in the S_1 lines will begin to saturate due to self-absorption at values of N that are five times smaller than the value of N required to saturate the weaker W lines. The ratio of the brightness in the W lines compared to the brightness in the S_1 lines, plotted versus N, is shown in Figure 6. We see that it should be possible to directly infer the column density N from the ratio of the brightnesses of the W and S_1 lines if the column densities are in the range $6 \times 10^{12} \lesssim N \lesssim 6 \times 10^{13}$.

The ratio of the brightnesses in the W and S lines shown in Figure 6 was calculated via an approximate method we shall describe here. The radiance Ri observed along a line-of-sight through the cloud is given by

$$4\pi Ri = B_i \, Noi \int S_u \, d\tau_i \, T(\tau_i)$$

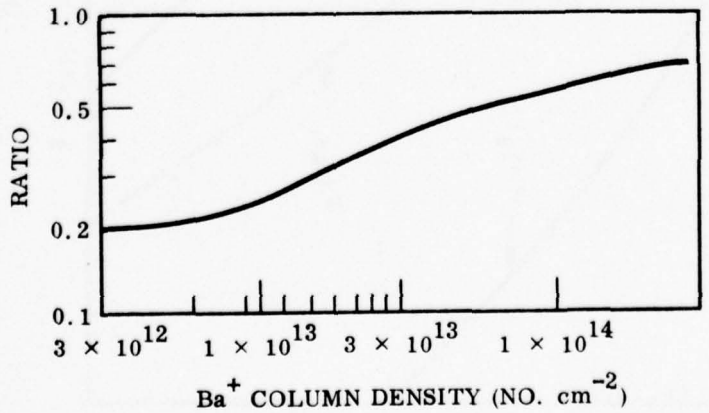

Figure 6. The ratio $R_{WS1} = R_{W7}/R_{S7} \simeq W(\tau_{W7})/W(\tau_{S7})$ plotted versus Ba^+ column density N.

where the $d\tau_i = nds/N_{oi}$; n is the Ba^+ number density; $d\vec{s}$ is an element of path length along the line of sight $\vec{s}$. S_u, the source function, is the fractional excitation rate in units cm^{-2} sec^{-1} (unit optical depth)$^{-1}$ to the upper state U; S_u is directly related to the volume excitation rate of upper state U, X_u, by $S_u = N_{oi} X_u / n$; B_i is the branching ratio for emission from upper state U into line i and $T(\tau_i)$ is the transmission function for resonance radiation given by

$$T(\tau_i) = \int_{-\infty}^{\infty} \frac{dx}{\sqrt{\pi}} e^{-\tau_i e^{-X^2}}$$

The integral $\int_0^t T(\tau')\, d\tau' \equiv W(\tau)$.

The ratio R_{WS_1} of the W lines to the S_1 lines is given by

$$R_{WS_1} = \frac{B_W N_{OW}}{B_{S_1} N_{OS_1}} \frac{\int d\tau_W T(\tau_W) S_U}{\int d\tau_{S_1} T(\tau_{S_1}) S_U}$$

In the approximation that S_U does not vary appreciably along the line-of-sight S, we obtain

$$R_{WS_1} \cong \frac{B_W N_{OW}}{B_{S_1} N_{OS_1}} \frac{W(\tau_W)}{W(\tau_{S_1})}$$

This approximation for R_{WS_1} is plotted in Figure 6. The approximation that S_u is constant is absolutely valid in the optically thin case.

We have established in section 2.3 that brightness data $4\pi R_W$ in the W lines can be used to determine N within 10% accuracy for transverse viewing (τ_W max $\lesssim$ 0.5) and about 30% for parallel viewing (τ_W max $\lesssim$ 1.0). Here in section 2.4 we have shown that the observed ratio of $R_{WS_1} = R_W/R_{S_1}$ might be utilized to improve on these estimates. In the next section we outline a method by which the accuracy to which N might be determined from the data will be greatly improved.

2.5 MORE SOPHISTICATED THEORY

In the approximation, S_u is constant over the cloud; $4\pi R_W$ is proportional to $W(\tau_W)$; and R_{WS_1} is proportional to $W(\tau_W)/W(\tau_{S_1})$.

In this approximation, N may be obtained directly from the data $4\pi R_W$ and R_{WS_1}. Unfortunately, S_u is not a constant in the optically thick case so we expect errors of the order 10 or 30% for transverse or parallel viewing geometries by using the simple expressions for $4\pi R_W$ and R_{WS_1} given above.

To obtain the S_u as a function of position in the cloud, one must modify the terms $N_L B_{LU} \rho_{LU}$ defined by Deuel and Sears (see Reference 1) in the following way:

$$N_L(\vec{r})\, B_{LU}\, \rho_{LU} \rightarrow N_L(\vec{r})\, B_{LU}\, \rho_{LU}\, T(\tau_{OLU})$$

$$+ N_L(\vec{r}) \cdot \int d^3\vec{r}' \;\; H(\vec{r}, \vec{r}')\, N_u(\vec{r}')$$

where τ_{OLU} is the optical depth in the transition from lower state L to upper state U along the path $\overline{O}(\vec{r})$ from the position $\vec{r}$ in the cloud to the sun, $T(\tau_{OLU})$ is the transmission function for resonance line radiation from the sun to point $\vec{r}$. The integral term accounts for absorption at point $\vec{r}$ due to emission from points $\vec{r}'$ in the cloud.

In the escape function approximation

$$\int d^3 r' H(\vec{r}, \vec{r}') Nu(\vec{r}') \cong N_L^{-1}(\vec{r}) [1 - E(\vec{r})] Nu(\vec{r}) A_{LU}$$

Here the escape function $E(\vec{r})$ is the probability that a photon emitted at point $\vec{r}$ will escape from the Ba^+ cloud rather than be absorbed at some point r' within the cloud. The escape function is easily computed via

$$E(\vec{r}) = \int \frac{d\Omega \hat{k}}{4\pi} T(Tr\hat{k}LU)$$

where the integral is taken over all directions of the unit vector $\hat{k}$, and the quantity $Tr\hat{k}LU$ is the optical depth for the LU transition along the direction $\hat{k}$ from point $\vec{r}$ to ∞. Clearly $E(\vec{r}) \leq 1$ and, for the optically thin case, $E(\vec{r}) = 1$.

Donahue and Meier (Reference 6) have shown that solutions obtained in the escape function approximation are accurate within a few percent for sunlit planetary atmospheres for moderate optical thicknesses $\tau \simeq 1$. We expect the escape function approximation to be even more accurate for application to sunlit release clouds with $\tau \simeq 1.0$. Certainly the escape function approximation will provide an approximation for the spatial dependence of S_u that is more accurate than the constant approximation discussed in section 2.4. By using the approximate spatial dependence for S_u we can obtain more accurately the dependence of R_{WS_1} on N.

The spatial dependence for the S_u may be obtained in the escape function approximation as follows. In Eqs. 7 through 11 in Ref. 1, we can replace the terms $N_L B_{LU} \rho_{LU}$ by $N_L(\vec{r}) B_{LU} \rho_{LU} T(\tau_{OLU}) + N_U A_{LU} [1 - E(\vec{r})]$ and obtain the spatially dependent solutions for the number densities in all the Ba^+ states. A reasonable first estimate $n_1(\vec{r})$ for the spatial distribution of Ba^+ ions may be

obtained by the approximation N_u/n_1 = constant (i.e., S_u = constant) from the spatially resolved data $4\pi R_W$ and R_{WS_1} and from knowledge of the diffusion coefficients.

The spatial variation we calculate for N_u^1/n by obtaining first iteration solution $N_u^1(\vec{r})$ of the modified Eqs. 7 through 11 of Reference 1 will allow us to interpret more accurately the data $4\pi R_W$ and R_{WS_1}. This will give us a second estimate $n_2(\vec{r})$ which is more accurate than $n_1(\vec{r})$. The procedure should rapidly converge to yield the $n(\vec{r})$ and $N_u(r)$ that are consistent with the spatially resolved data $4\pi R_W$ and R_{WS_1}.

In sections 2.3 and 2.4 we showed how we could use the spatially resolved brightness data $4\pi R_W$ and ratio R_{WS_1} to obtain spatially resolved column densities N accurate within about 10% for transverse viewing geometry. Here in section 2.5 we have shown a simple way to improve on this accuracy and to verify that the column densities N we obtain are consistent with the spatially resolved optical data $4\pi R_W$ and R_{WS_1}.

2.6 CONCLUSIONS

We have shown that with instrumental spectral resolution FWHM $\Delta\lambda_I \simeq 0.01$A it is possible to resolve the W and S lines in the Ba^+ hyperfine structure. We have also shown that by measuring the absolute brightness in these resolved lines it is possible to infer line-of-sight column densities N through the Ba^+ cloud with accuracy much better than 10% for viewing geometries transverse to the magnetic field and 30% for parallel viewing. Sophisticated analysis is necessary to extract the desired information Ba^+ column densities N from the data (brightnesses in the resolved hyperfine lines). We note that, if for some unforeseen reason the W and S_3 lines cannot be resolved, it is still possible to utilize the analysis developed in section 2.5 to the sum of the brightnesses in these lines and the ratio of this sum to the sum of the brightnesses in the S_2 and S_1 lines, in order to accurately obtain the Ba^+ column densities for the release size under consideration for this experiment.

Section 3
TIFIS* DESIGN SPECIFICATIONS

3.1 INTRODUCTION

It was demonstrated in the introduction and in the theoretical sections that measurements of the emission intensity of the barium ion resonance line at 4934 Å having spectral resolution of 0.01 Å will allow determination of the Ba ion column density in the cloud. This measurement must be made with a spatial resolution of about 30 m at the cloud (about 10^{-4} rad). These two specifications place extremely stringent requirements on the design of a TIFIS system in that every high sensitivity and very high photon counting efficiency are required to meet these specifications concurrently.

In this section, we treat the experimental design of the TIFIS. The system is described according to its separate subunits: Section 3.2 contains a description of the parameters of the telescopic objective system; section 3.3 describes the Fabry-Perot interferometer and forefilter unit; section 3.4 describes the intensified detector imaging system and data system; and the supporting optical subsystems and the tracking mount are discussed in section 3.5.

3.2 TELESCOPE SYSTEM SPECIFICATIONS

The photon collection efficiency of the telescope essentially controls the detectability of the Ba ion cloud and the signal-to-noise ratio of the measurements. Other important parameters of the system are the optical transmission, the quantum efficiency of the detector, the angular diameter of the spatial resolution element

*Telescopic Intensified Fabry-Perot Interferometer System.

required, and the spectral resolution of the Fabry Perot interferometer. All these parameters are interrelated; however, we begin by describing the optical collection system because of the existing DNA-owned Cassegrain telescope and tracking mount system. The specifications of this telescope are listed in Table 3 below.

Table 3. Cassegrain Telescope Specifications.

Parameter	Specification
Diameter	46 cm
Focal length (effective)	267 cm
F number	5.8
Exit beam diameter	10.2 cm
Collector area (minus obscuration)	1460 cm^2
Figure	Cassegrain (Dahl-Kirkham)

The photon collection efficiency of a telescopic system working into a photoelectric detector is given by the formula:

$$C = A \Omega Q T I \qquad (3.1)$$

where

- C = detected count rate, photoelectrons/sec
- A = collector area
- Ω = solid angle of the resolution element
- Q = quantum efficiency of the detector
- T = transmission of the optical system
- I = intensity of the source

Conservative values of 10% have been chosen for Q and T. The solid angle, $\Omega = 8 \times 10^{-9}$ sr, is that for the smallest picture element size (pixel), 10^{-4} rad,

which is appropriate for 30-m spatial resolution on a cloud at slant range of 300 km. The pixel size may be somewhat larger during a portion of the measurements when the Ba ion cloud is closer.

Using the telescope specifications contained in Table 3, we find the count rate per pixel second for a given Ba ion cloud emission intensity (expressed in Rayleighs). This value is 9.6 photocounts-sec^{-1}-pixel^{-1} × (kiloRayleigh^{-1}).

The emission intensities for Ba II clouds versus time after release have been measured for a number of SECEDE II events (see Reference 2 for example). These experiments, conducted at Eglin AFB, Florida, are representative of the cloud ion yield, altitude, and geometry of the STRESS experiments. Figure 7 illustrates the brightness history of some of these events in the 4934 Å resonance line as obtained by Hake (Reference 2). We have added a brightness scale in kiloRayleighs and a count rate scale to correspond to the system as described above. It is clear from this figure that a reasonably high count rate exists (about 1000-cts-sec^{-1}-pixel^{-1}) for a time span of 20 min or so after release. This emission rate is spread out among the spectral resolution elements in the main and hyperfine components of the 4934 Å complex. However, because of the large optical depth and self-absorption of the main 4934 Å line during much of the measurement, we expect a substantial fraction of the emission to be in the S_1, W, and S_2 and S_3 regions, as discussed in Section 2.

3.3 FABRY-PEROT INTERFEROMETER AND FOREFILTER SPECIFICATIONS

The Fabry-Perot interferometer provides the spectral dispersive element for the TIFIS optical system. The design of the Fabry-Perot interferometer and forefilter subsystem requires optimization of a complicated set of interdependent specifications relating telescope size and focal length, interferometer size and resolution, and forefilter size and resolution. The specifications required by the STRESS experiment are: 30-m spatial resolution at the cloud (10^{-4}-rad resolution element), 0.01 Å spectral resolution, and a field-of-view at the cloud sufficient to encompass several Fresnel

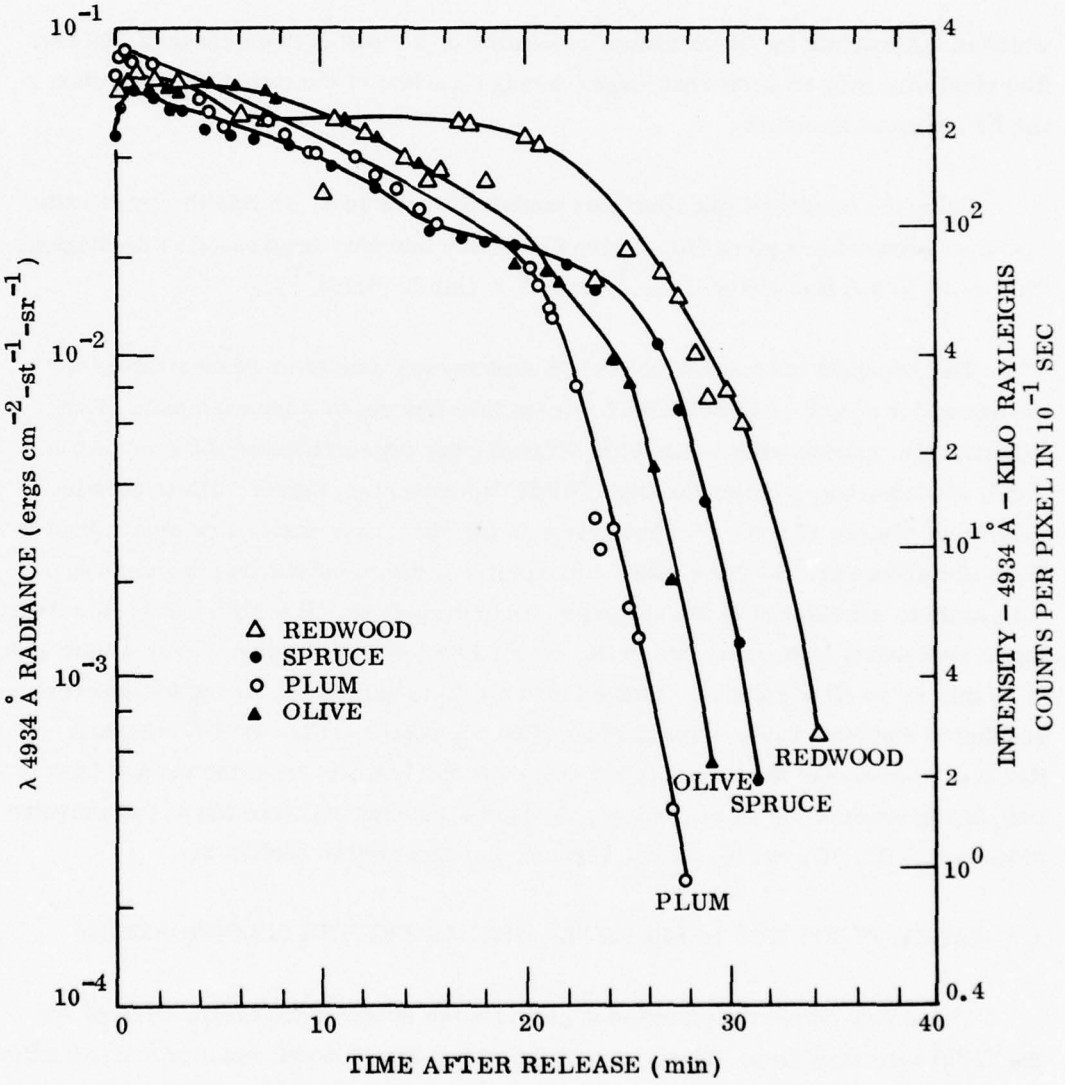

Figure 7. Measured intensities in 4934 Å lines for SECEDE II events. Note that events SPRUCE and PLUM are about same size and altitude (185 km) as planned STRESS events.

zone sizes. A field-of-view, FOV = 5 mrad, satisfies this requirement. This section describes how these specifications can be met by the existing DNA Fabry-Perot interferometer (see Fig. 8) with minor modifications to its optical system in order to couple it to the 18-in. telescope.

The spectral resolution of the Fabry-Perot interferometer is related to the other parameters of the system by the following equations:

$$F = FSR/\Delta\lambda \tag{3.2}$$

$$FSR = \lambda^2/2nd \tag{3.3}$$

$$\Delta\lambda/\lambda = \Phi^2/2n^2 \tag{3.4}$$

where

- F = finesse of the instrument
- FSR = free spectral range
- λ = wavelength of the emission to be measured
- d = distance between etalon plates
- n = index of refraction of the interplate material ($n = 1$, for air)
- Φ = acceptance angle of the instrument at the dispersive element
- $\Delta\lambda$ = spectral resolution element

The finesse of the instrument is controlled by the flatness of the optical plates and coatings and by the reflectivity of the coatings. Typical values of finesse range around 20 for a good quality etalon. The free spectral range, which is the only adjustable parameter given a required resolution and a finesse, is selected by varying the spacing of the etalon plates. For a nominal finesse of 20, and a required spectral resolution of 0.01 Å, the free spectral range required is thus 0.2 Å, and the plate spacing for air-separated plates is 5 mm.

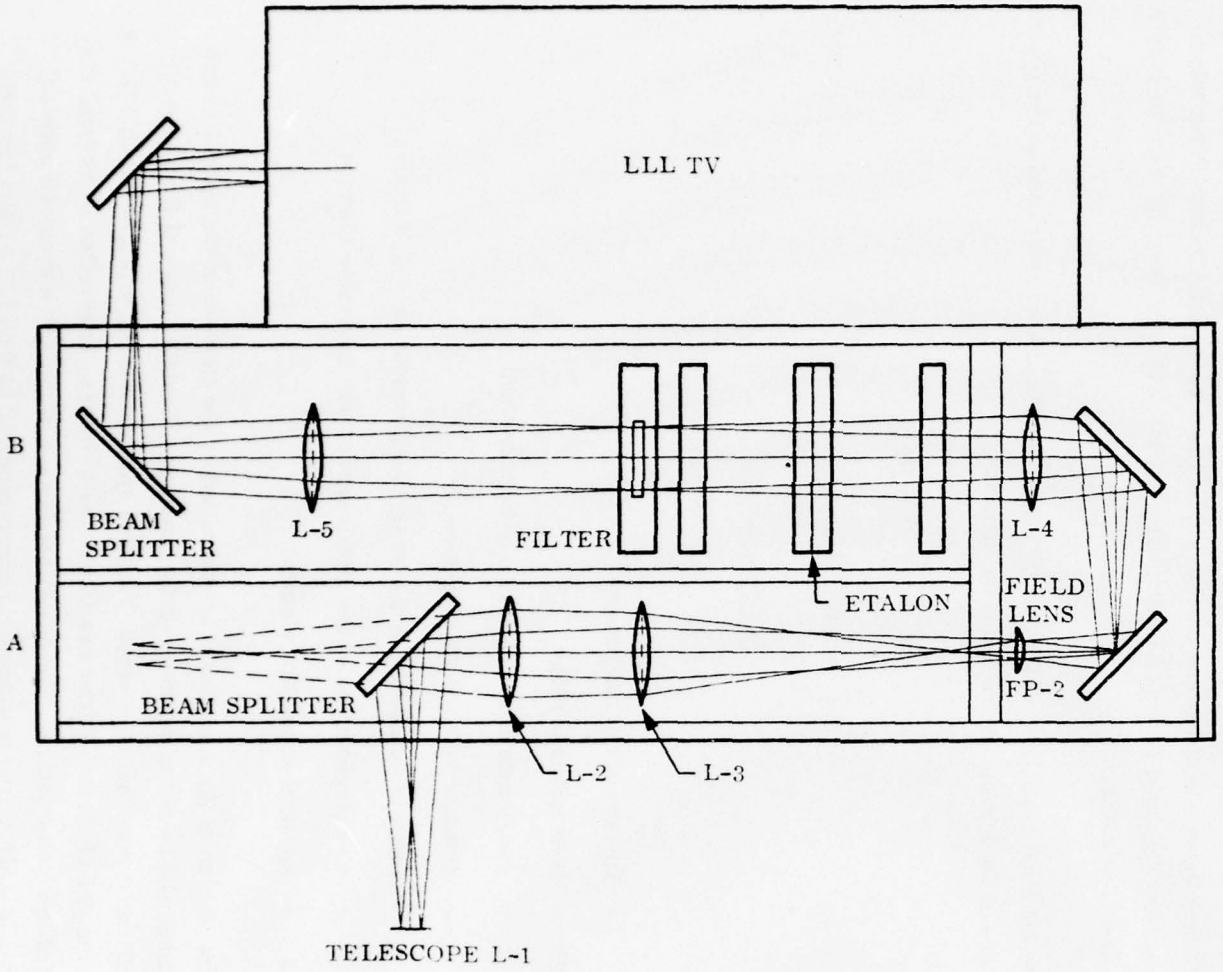

Figure 8. Final optical design for the TIFIS Instrument. A calibration light source with U.S. Air Force resolution targets at position A. The photometric detector PM tube is attached at position B

Another constraint upon selection of the Fabry-Perot system parameters is the maximum angular resolution element required by the measurement. Because the spectral resolution of the etalon depends upon the angular spread of the ray bundle which passes through it according to formula (3.4), we see that a maximum spatial resolution element exists for a given value of spectral resolution. In our case, the angular resolution element defined by the spectral resolution of 0.01 Å is $\Phi = 2$ mrad. Because our stated spatial resolution element is only 10^{-4} rad, we are able to optically fold the beam by a factor as large as 40 using telescopic collection optics. The actual beam folding factor that was used is approximately 10. The reasons for this will be discussed later.

Use of the television imaging technique as opposed to monitoring the fringe shape for a single pixel, as has previously been done by Sears (Reference 1) and by Hake (Reference 2), allow more information about the spatial structure of the cloud to be obtained, without the disadvantage of having to scan the cloud by using the tracking mount. Such a technique multiplies the information output rate considerably, thus improving the statistical properties of the data as applied to both the spectral analysis and to the spatial distribution analysis. However, use of this technique imposes additional constraints upon design of the Fabry-Perot system. Not only the single pixel of 10^{-4} rad must be passed through the etalon, but the spatial distribution of emission intensity in second, third, and higher order rings or interference fringes must image meaningful parts of the field-of-view at the cloud. Additionally, this image must be transferred to the TV detector with adequate resolution. For a TV scan having 256 horizontal and vertical resolution elements, not more than 25 fringes, each having 10 spectral elements, could be imaged without loss of information if equally spaced across the raster. Actually, the fringe pattern becomes successively more closely spaced as the order increases (i.e., the distance from the central order fringe) such that the outermost fringes will not be resolved adequately. Therefore, the total number of fringes which can be imaged is limited by practical considerations on image transfer. The fringe spacing is controlled by Eq. (3.4) where the resolution element $\Delta\lambda$ is now taken as the free spectral range of the etalon (0.2 Å) multiplied by the

integer order number. The angle determined by Eq. (3.4) then is the off-axis angle of the nth order ray passing through the etalon. Table 4 lists the off-axis rays through the etalon for orders up to 10 and also includes the projected off-axis angle through the telescope. The latter angle represents the portion of the cloud which is imaged through the Fabry-Perot in successively higher order interference fringes. Clearly, the total field-of-view possible through a telescopic system is strongly limited by the total number of fringes which can be successfully imaged and resolved on the detector. This in turn is controlled by the beam reduction ratio (i.e., the magnification between the telescope and FPE). We have chosen a beam reduction ratio of 10 which provides a total field-of-view of 5 mrad and a ring pattern out to 7th order, as optimum for our requirements. It should be noted that 5 mrad does not cover the entire cloud diameter, but does cover about four times the largest Fresnel zone size for the STRESS experiment.

Table 4. Off-axis ray interference fringe position

Order	$\Delta\lambda$	Φ (Off-Axis Angle at FPE) (rad)	Φ' (At Cloud) (rad)	Φ' (deg)
1	0.2 Å	8.9 (-3)[a]	8.9 (-4)	0.06
2	0.4	1.3 (-2)	1.3 (-3)	0.075
3	0.6	1.5 (-2)	1.5 (-3)	0.085
4	0.8	1.8 (-2)	1.8 (-3)	0.10
5	1.0	2.0 (-2)	2.0 (-3)	0.11
6	1.2	2.2 (-2)	2.2 (-3)	0.12
7	1.4	2.4 (-2)	2.4 (-3)	0.13
8	1.6	2.6 (-2)	2.6 (-3)	0.14
9	1.8	2.7 (-2)	2.7 (-3)	0.15
10	2.0	2.8 (-2)	2.8 (-3)	0.16

(a) (-x) indicates 10^{-x}

The forefilter specifications are dependent upon the required spatial resolution, the total field-of-view, and the forefilter must pass the requisite number of orders of interference through the FPE. The acceptance cone of the collimating lens (see Figure 8) is controlled by the image size at the first focal plane and by the f/number of the lens. We wish to preserve all of the light gathered by the primary telescope, therefore the collimator f/number must be less than or equal to 5.8. Finally, the overall collimated beam diameter must not exceed the usable diameter of the FPE and the forefilter which is 4 to 5 cm. The image size at the first focal plane is 13 mm. If we choose a lens focal length of 25 cm, then the half angle of the input cone is 0.025 rad. Using Eq. (3.4), we find a minimum value for forefilter spectral resolution of 0.8 Å or four free spectral ranges of the FPE. As previously discussed, the FPE ring pattern must pass up to seven orders, i.e., 1.4 Å; therefore, the acceptance cone angle of the collimator does not limit the system. It was necessary, however, to choose a wider forefilter spectral resolution based upon practical considerations of cost versus resolution available in fixed passband filters.

After passage through the forefilter and FPE units, the collimated beam is reimaged onto the detector photocathode using a 400-mm telephoto lens. The detector system, an image intensified integrating TV camera, is described in the following section.

3.4 INTENSIFIED IMAGING SYSTEM

The imaging system plus the digital and analog data processing electronics are illustrated in Figure 9. The image obtained from the Fabry-Perot interferometer subsystem is focused on a Varo Image Intensifier which is coupled by fiber optics to a Westinghouse SEC type vidicon. This SEC tube is a charge integrating storage tube permitting long exposures in order to accumulate photon count statistics. In this type of tube the exposure is limited mainly by the dark emission of the photocathode; however, exposures of 10 seconds or longer do not suffer from loss of picture quality. During an exposure, the TV vidicon beam is cut off and the charge pattern produced by

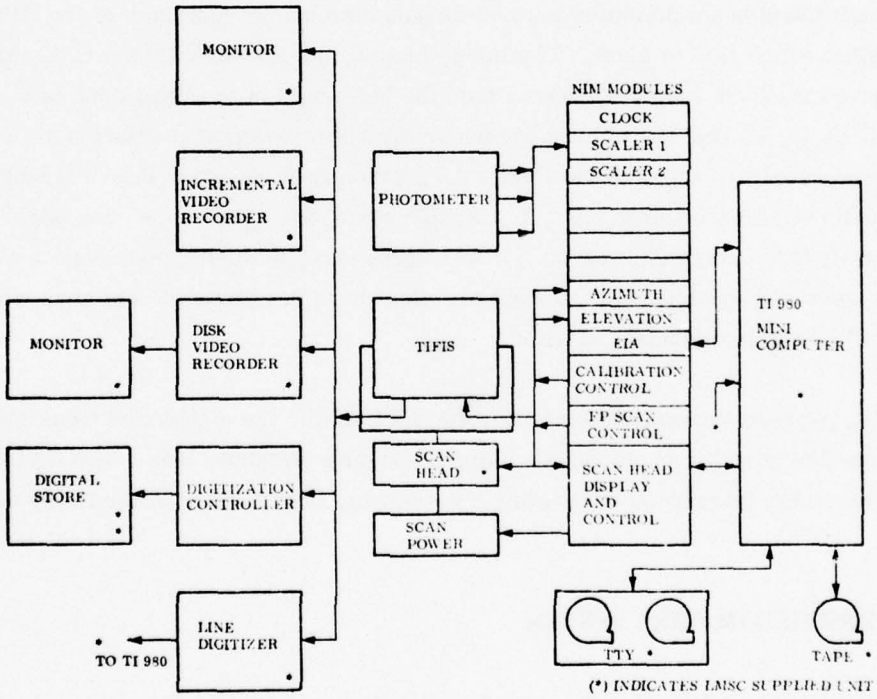

Figure 9. TIFIS data and control electronics subsystem. TI980 mini computer plus video control and recording electronics were supplied by LMSC.

the intensified image begins to accumulate on the target. After the exposure is terminated, the video processing data system is commanded by the TI980 minicomputer to receive data from the camera tube. This step is initiated by the next TV frame synch signal. The current generated during the discharge of the target by the scanning beam is the video signal which is proportional to the accumulated charge. Good linearity between the video signal and the input light intensity exists after preparation or conditioning of the target.

For the purpose of Ba ion cloud calibrations, a Ba lamp spectral calibration source will be included such that each frame will have the intensity of the Ba high-resolution spectrum included. Preprogrammed exposure sequences can be generated and controlled by means of the computer, or the video signal itself can be used to generate the exposure time sequence. For Ba ion cloud measurements, both techniques may be used, depending upon the range of Ba ion cloud intensities expected and their rate of temporal variation.

The output data therefore consist of a series of successive pictures of the Ba ion cloud divided into concentric spatial fringes which are slowly scanned in wavelength through the complex spectral emission pattern of the Ba 4934 Å line. Any given video frame will allow measurement of the horizontal structure of the Ba ion column density through the cloud in a series of concentric cuts. From these patterns, the striation thickness and column depths may be determined as discussed in the theoretical section.

In addition to the overall optical and electronic design effort, the system operation against a simulated structured ion cloud was computed. Here, we assumed a k^{-2} spatial spectrum for clouds having 100-kR and 10-kR mean intensity and 20-km characteristic size. The theoretical values of power spectral density (cts/km) based upon system idealized modulation transfer function (MTF) detector sensitivity, and noise levels were computed. These two cases are illustrated in Figure 10 where an MTF corresponding to an 8-m (0.025-mrad) resolution element is assumed. From Figure 10 we see that spatial scales as small as 30 m may be resolved at early times when the cloud

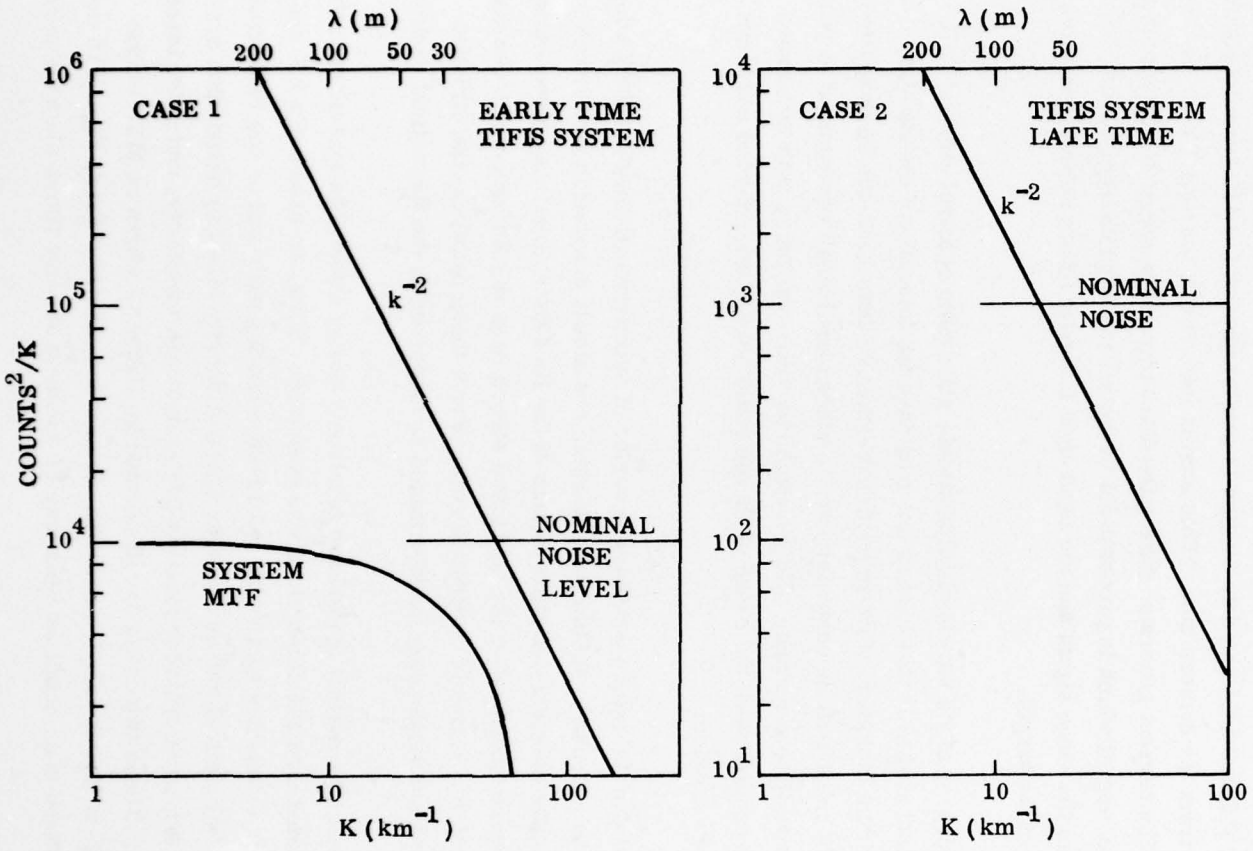

Figure 10. Calculated TIFIS system response to 4934 Å ion cloud emission irregularity spectrum following a k^{-2} spectrum. *Idealized system MTF computed for 8-m resolution at cloud.* Cloud mean intensity at early times in 100 kR, at late times is 10 kR.

is bright (100 kR at 4934 Å). At later times, attainable resolution is poorer but still should approximate 100 m or so for a cloud as faint as 10 kR in 4934-Å emission.

3.5 SUPPORTING OPTICS AND TRACKING MOUNT

Two optical measurements are required for support of the TIFIS system: a boresighted 4934-Å photometer to provide absolute photometrically calibrated measurements of the entire 4934 Å line system, and a TV tracking camera which can show the overall position of the Ba ion cloud and the boresighted position of the TIFIS field-of-view. Additionally, to support the entire optical instrument complement and provide high-resolution spatial position information, a tracking mount is required.

A filtered low light level TV system may be boresighted to the TIFIS system for tracking purposes. Because this system has a much larger field-of-view (i.e., about 10°) and much larger resolution elements (i.e., 10^{-3} rad), much more light is available for purposes of imaging the position of the overall ion cloud. Such a TV camera was available but proved to be inoperative just before shipment of the system. A similar camera was borrowed from TIC (Technology International Corporation) and installed in the field to assist in covering events ESTHER and FERN.

An auxiliary photometric output capability was incorporated into the TIFIS instrument in order to provide cloud intensity calibrations. Fig. 8, position B shows the location of the photometer output which images only the central order fringe through a pinhole onto the photocathode. In this manner, we are able to obtain both radiometric calibration and line shape information.

The TIFIS system plus its supporting optical units was mounted on a modified searchlight head. This unit was modified to carry the 18-in. Cassegrain telescope. Minor modification to the tracking mount and telescope cell allowed direct coupling

to the FPE etalon and forefilter optical subsystem, and to the image-intensified TV subsystem. The tracking mount is positioned by means of digitally controlled stepping motors in azimuth and elevation axes. The stepping motors can also be controlled by an online minicomputer (TI980B, LMSC owned). Absolute position information was derived from shaft encoders. Several modes of control were designed into the system. Manual, joy-stick control, prepositioning, and preset scan modes were incorporated as well as a computer-derived control mode. Using the latter mode, tracking of a satellite or rocket trajectory would be possible, given the proper input trajectory information to the computer. The control modes are intended to be as flexible as possible in order to allow maximum data acquisition under a variety of different experimental requirements.

Section 4
SUMMARY OF FIELD OPERATIONS AND DATA ACQUISITION

In this section we present a chronological summary of the operations at the field site at Tyndall AFB, Florida, and provide an estimate of the data acquisition success for each event. Unfortunately, at the time of writing this report, the instrumentation van and data have only just been returned from the field, hence a more detailed quick-look assessment of the data cannot be provided.

The TIFIS instrument was shipped to the field in February 1977. The field site was opened by R. D. Sears and R. Reeves on 8 February. Mechanical installations in support of the instrumentation were completed that week. The TIFIS instrument, supporting electronics, and instrumentation van arrived a number of days late on 14 February. Installation of the electronics and adjustment of the electronic and optical componentsproceeded during that week. Dr. S. Mende arrived on 18 February and assisted in completing the installation of the electronics, in completing the computer program debugging, and in final overall system adjustment.

The TIFIS system was initially ready for the opening of the shot window on 23 February; however, a succession of problems interfered with full utilization of the system during the first few shots. Operation of the system during the five barium releases and the problems encountered are summarized as follows:

- Event BETTY: Launched 26 February during cloudy conditions at Tyndall AFB. No data obtained because of heavy clouds and intense moonlight.
- Event CAROLYN: Launched 2 March. There were problems in acquiring and tracking useful portions of this cloud because the phenomenology was not as expected and because the site was undermanned (only one operator instead of the two desired). Only partial data acquisition.

- Event DIANNE: Launched 7 March. Problems as above, except that a manual tracking mount controller helped in tracking the cloud at late times. Only partial data acquisition. After this event, realignment of some of the subsystem controls was done to allow more effective one-man operation of the system.
- Event ESTHER: Launched 13 March. Addition of a wide-field TV camera on the mount (borrowed from TIC) assisted greatly in acquisition of the cloud at early times and in late time tracking. Essentially complete data coverage. This event provided the most interesting striation morphology.
- Event FERN: Launched 14 March. Again, good striation phenomenology was observed and essentially complete data acquisition was attained. For both events ESTHER and FERN, the cloud intensity was low due to the pre-sunset launch time, e.g., the clouds were about 90 min old when acquired at sunset. This required integration times as long as 5 sec (300 TV frames).

In both events ESTHER and FERN there was strong indication of structure in the ionized cloud at least as small as 0.1 x the TIFIS FOV, e.g., 0.5 mrad.

After completion of the FERN experiment, the TIFIS system was packed, loaded into the instrumentation van and made ready for shipment from the field. The TIFIS system was returned to Palo Alto on 4 April 1977.

Section 5
QUICK-LOOK DATA ASSESSMENT

In the time period between the physical return of the TIFIS instrument and its associated data reduction apparatus and the date of this report, a limited degree of data examination and reduction has occurred. We are unable to present calibrations and digital housekeeping data because the Texas Instrument minicomputer was apparently damaged during its return shipment. We have viewed the imaging data from the four observed events, the operational details of which are summarized in the previous section. In this section we present some preliminary efforts at producing imaging data for event ESTHER which shows indications of small-scale spatial structure.

The overall data processing scheme is illustrated in Figure 11, which covers procedures which we will follow for both digital and imaging data. A number of frames of imaging data have been processed using the LMSC RTIP (real time image processor) in which simple averaging has been carried out in order to reduce the noise in the imaging data. The RTIP images of the USAF resolution target are illustrated in Figure 12. Here, the RTIP averaged five frames of data obtained during the test target calibration run after event ESTHER. The integration times were the same as for event ESTHER data to be presented, i.e., 5 sec. Figure 12 clearly shows that the spatial resolution of the TIFIS system is approximately 0.2 mrad or better, which approaches its design goals. A better measurement of the modulation transfer function of the TIFIS instrument will be derived from further study of these target patterns.

Imaging data from event ESTHER are illustrated in Figures 13 and 14 which show a sequence of 5-sec integrations on the ESTHER ion cloud in the region of the coronal striation structure. Inhomogeneities in the intensity of the Fabry-Perot ring structure indicate that small-scale structure was detected. Although the photographic reproductions do not present a clear indication of the scale sizes and orientations, magnetic

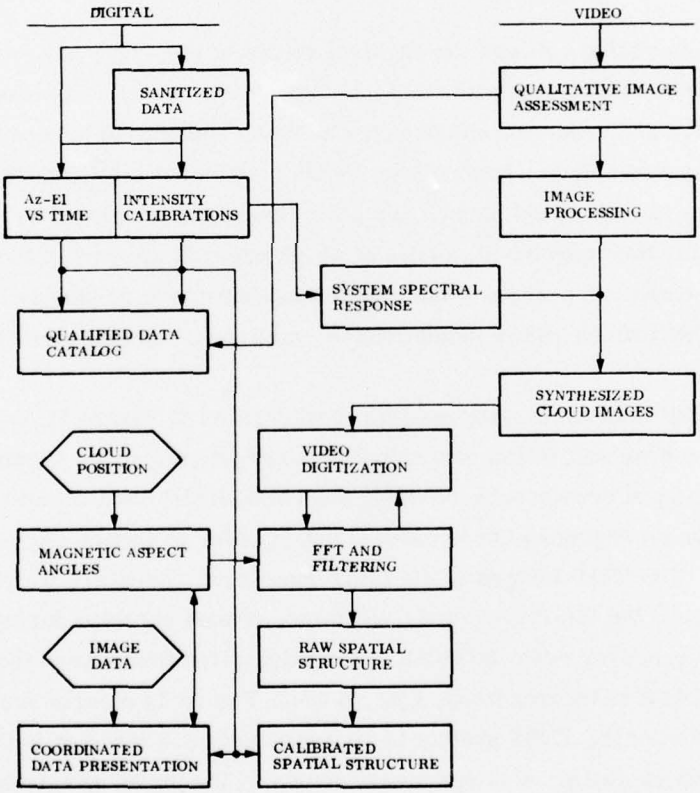

Figure 11. Block diagram of TIFIS data reduction, evaluation, and assessment procedure. This process will be applied to STRESS events CAROLYN through ESTHER as resources permit.

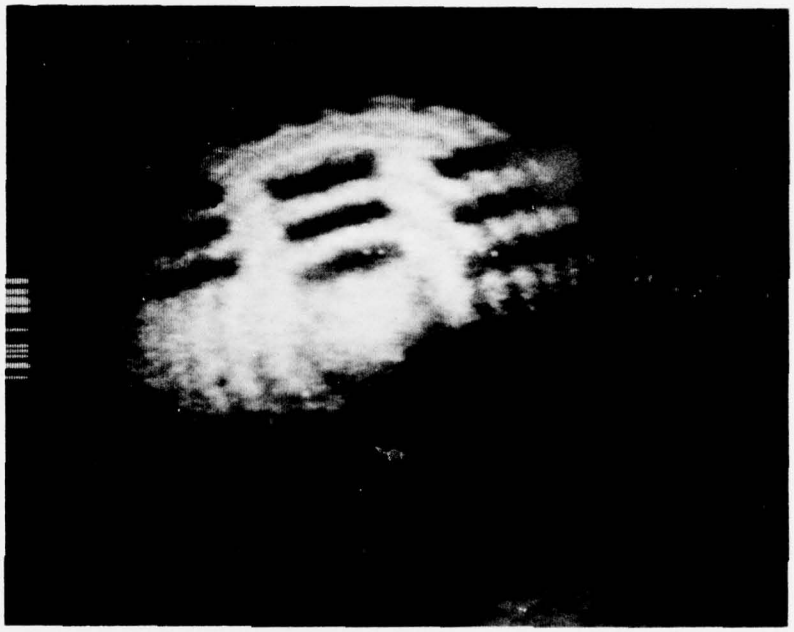

Figure 12. Air Force resolution target viewed through TIFIS system. Total field of view is 5 mrad. Target bars at upper half of picture are 0.5 mrad center to center.

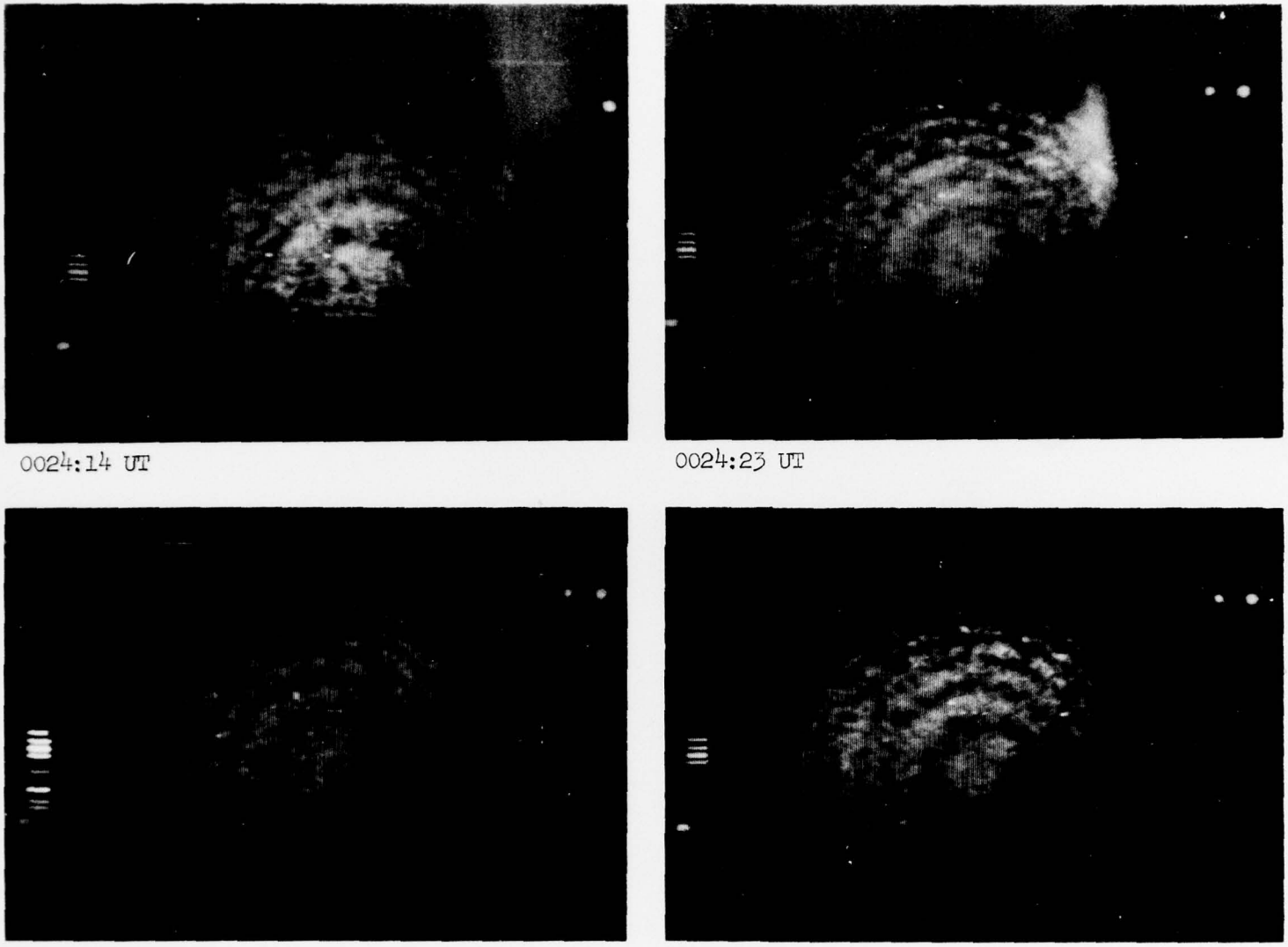

Figure 13. Sequence of TIFIS images observed for event ESTHER. Integration time is 5 sec per image. Fine-scale structure may be seen modulating Fabry-Perot fringe pattern intensity in upper half of images.

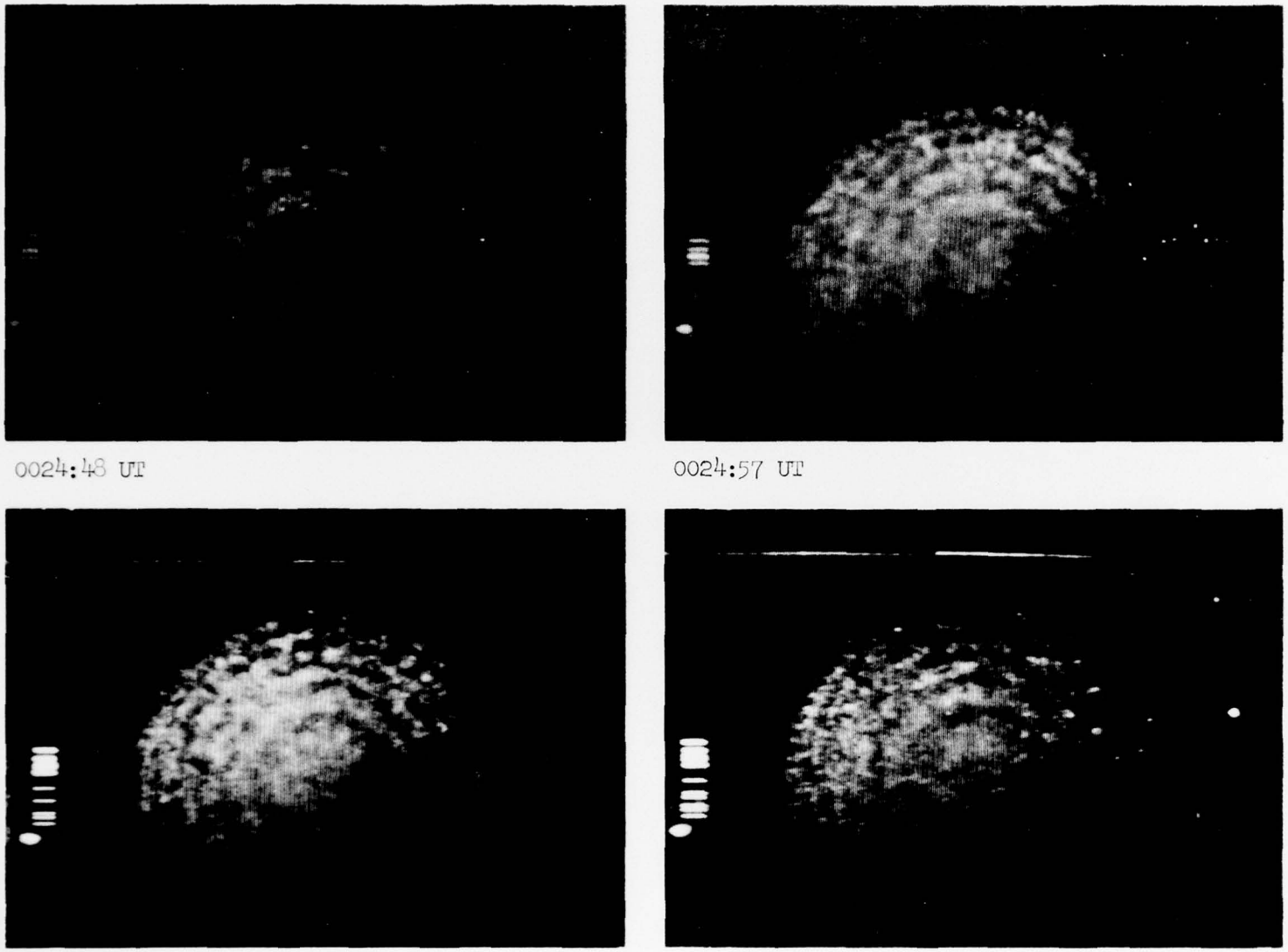

Figure 14. Sequence of TIFIS images observed for event ESTHER. Integration time is 5 sec per image. Fine-scale structure may be seen modulating Fabry-Perot fringe pattern intensity in upper half of images.

field direction in roughly the upper-left to lower-right portions of the pictures agrees with the apparent direction of the irregularities. Scale sizes at least as small as one tenth of the field-of-view, or 0.5 mrad, are observed. These scales would correspond to horizontal dimensions of 100 to 200 m at the cloud for this event.

As indicated in Figure 11, a much more intensive procedure for image processing and assessment of the data is required before the irregularity scales, barium ion cloud column density, and other quantitative parameters can be specified in detail. However, imaging data observed to date indicates that at least for events ESTHER and FERN the small-scale inhomogeneities were observed and were successfully recorded for useful portions of the ion cloud lifetimes.

Section 6
REFERENCES

1. Sears, R. D., and Deuel, R. F., "Interferometric Measurements on SECEDE I Barium Releases," RADC TR 68-465, September, 1968
2. Hake, R. D., Jr., "SECEDE II Fabry-Perot Interferometer Data," RADC 72 242, July 1972
3. Fischer, W., Hartmann, M., Huhnermann, H., and Vogg, H., Zeit Physik 267, 209, 1974
4. Kelly, F. M., and Tomchuck, E., Can. J1. Physics 45, 3931, 1967
5. Gallagher, A., Phys. Rev. 157, 24, 1967
6. Donohue, T. M., and Meier, R. R., J. Geophys. Res. 72, 2803, 1967

DISTRIBUTION LIST

DEPARTMENT OF DEFENSE

Defense Documentation Center
Cameron Station
12 cy ATTN: TC

Director
Defense Nuclear Agency
ATTN: TISI, Archives
3 cy ATTN: TITL, Tech. Library
ATTN: DDST
ATTN: RAAE

Dir. of Defense Research & Engineering
Department of Defense
ATTN: S&SS (OS)

Commander
Field Command
Defense Nuclear Agency
ATTN: FCPR

Chief
Livermore Division, Field Command, DNA
Lawrence Livermore Laboratory
ATTN: FCPRL

DEPARTMENT OF THE ARMY

Commander/Director
Atmospheric Sciences Laboratory
US Army Electronics Command
ATTN: DRSEL-BL-SY-S, F. E. Niles

Commander
Harry Diamond Laboratories
ATTN: Mildred H. Weiner, DRXDO-TI
ATTN: Francis N. Wimenitz, DRXDO-NP

Commander
US Army Foreign Science & Tech. Center
ATTN: P. A. Crowley

DEPARTMENT OF THE NAVY

Commander
Naval Electronic Systems Command
Naval Electronic Systems Command Hqs.
ATTN: PME 117-T, Satellite Comm. Project Off.

Director
Naval Research Laboratory
ATTN: Code 7700, Timothy P. Coffey

Officer-in-Charge
Naval Surface Weapons Center
ATTN: Code WA501, Navy Nuc. Prgms. Off.

DEPARTMENT OF THE AIR FORCE

AF Geophysics Laboratory, AFSC
ATTN: OPR, James C. Ulwick
ATTN: SUOL, Rsch. Lib.

DEPARTMENT OF THE AIR FORCE (Continued)

AF Weapons Laboratory, AFSC
ATTN: SUL
ATTN: DYC, Captain L. Wittwer

Air Force Avionics Laboratory, AFSC
ATTN: AAD, Allen Johnson

SAMSO/SK
ATTN: SKA, Lt Toni Clavin

ENERGY RESEARCH & DEVELOPMENT ADMINISTRATION

EG&G, Inc.
Los Alamos Division
ATTN: James R. Breedlove

Los Alamos Scientific Laboratory
ATTN: Doc. Con. for John Wolcott

OTHER GOVERNMENT AGENCY

Department of Commerce
Office of Telecommunications
Institute for Telecom Sciences
ATTN: William F. Utlaut

DEPARTMENT OF DEFENSE CONTRACTORS

Aerospace Corporation
ATTN: D. P. Olsen, 120, Rm. 2224E

ESL, Inc.
ATTN: C. W. Prettie

General Electric Company
TEMPO-Center for Advanced Studies
ATTN: DASIAC

Institute for Defense Analyses
ATTN: Ernest Bauer
ATTN: Joel Bengston

Jaycor
ATTN: S. R. Goldman

Lockheed Missiles & Space Company, Inc.
ATTN: Robert Sears
ATTN: J. B. Kumer

M.I.T. Lincoln Laboratory
ATTN: Lib. A-082 for David M. Towle

Mission Research Corporation
ATTN: Ralph Kilb

Physical Dynamics, Inc.
ATTN: Joseph B. Workman

R & D Associates
ATTN: Bryan Gabbard
ATTN: Robert E. Lelevier

The Rand Corporation
ATTN: Cullen Crain

DEPARTMENT OF DEFENSE CONTRACTORS (Continued)

Science Applications, Inc.
ATTN: Lewis M. Linson

DEPARTMENT OF DEFENSE CONTRACTORS (Continued)

SRI International
ATTN: Walter G. Chestnut
ATTN: Dan McDanial